Title
Characterization of Nonporous and Porous Hyaluronic Acid Hydrogels and Their Partial Degradation to Enhance Transfection In Vitro

Author
Miller, Andrew William

Publication Date
2018

Peer reviewed|Thesis/dissertation

UNIVERSITY OF CALIFORNIA

Los Angeles

Characterization of Nonporous and Porous Hyaluronic Acid Hydrogels and Their Partial Degradation to Enhance Transfection *In Vitro*

A thesis submitted in partial satisfaction

of the requirements for the degree Master of Science

in Chemical Engineering

by

Andrew William Miller

2018

ABSTRACT OF THE THESIS

Characterization of Nonporous and Porous Hyaluronic Acid Hydrogels and Their Partial Degradation to Enhance Transfection *In Vitro*

by

Andrew William Miller

Master in Chemical and Biomolecular Engeering

University of California, Los Angeles, 2018

Professor Philippe Sautet, Chair

Hydrogels have presented themselves as attractive options for temporary tissue replacement after wound as they provide moisture and protection for the affected area; meanwhile, therapeutics can also be loaded into hydrogels to positively influence wound repair. However, cell access to these therapeutics can be limited if the polymer network is too tight. This work presents a partially-degraded, DNA-loaded hyaluronic acid (HA) hydrogel for enhanced *in vitro* transfection. The partial degradation is hypothesized to loosen the polymer network to allow for greater cell infiltration and access to the loaded DNA. Thorough characterization is performed on this type of gel to ensure system robustness; measurements include rheology, void fraction, cell seeding, and mesh size. This work reports enhanced transfection and cell infiltration for partially degraded, nonporous, DNA loaded HA gels with groundwork placed for expansion to a porous structure.

The thesis of Andrew William Miller is approved.

Yvonne Chen

Tatiana Segura

Philippe Sautet, Committee Chair

University of California, Los Angeles

2018

Dedications

I would like to dedicate this thesis to all of those who supported me for the past two years including my family and Dr. Segura, whose unwavering encouragement and support often propelled me forward.

Table of Contents

Table of Figures

1 Introduction

The body has a variety biochemical cascades responsible for wound healing; however, certain tissues and diseased patients experience slowed or delayed wound recovery. In 2014, 108,000 diabetic patients were subject to lower extremity amputation due to chronic wounds [1]. To combat chronic wounds, reduce patient loss of limb, and improve quality of life many therapeutic biomaterials and techniques have been introduced throughout the years. Some of these techniques or materials include hyperbaric chambers and a multitude of biomaterial dressings whose compositions vary greatly including: chitosan, hyaluronic acid (HA), collagen, nylon, silicone etc.[2-4]. One of the main themes of these biomaterials is their ability to ensure hydration and sterility while also providing stability and/or nutrients to the wound site. Enhancing the wound sites' access to required nutrients permits local cells to thrive and replenish the missing tissue. As wound healing is an energy intensive process, wounded tissue cells' access to plentiful amounts of oxygen is crucial for proper and timely tissue regeneration[5, 6].

Alternative to dressings, external therapeutic treatments including hyperbaric oxygen chambers (HBO) or topical oxygen (TO) strive to satisfy the oxygen needs of regenerating tissues, but is not widely accepted, access can be limited, and can be uncomfortable for the patient. HBO has even had cases of supersaturation with oxygen, potentially damaging the healing tissue[5, 6]. Rather than apply oxygen from outside the body, angiogenic biochemicals can be used to promote blood vessel formation within the wound bed ultimately providing the regenerating tissue with not only oxygen but other required nutrients and cells required for wound healing. These bioactive molecules associated with would repair include chemokines, integrins, and various growth factor proteins[4, 7, 8].

Incorporation of these bioactive molecules into a matrix has recently increased in popularity. This matrix not only houses the therapeutic molecules, but also maintains wound moisture, facilitates cell adsorption, and localizes the release of said therapeutic over time[4]. Increasing the concentration of these bioactive molecules in the wound bed can be achieved in a variety of different ways; however, localized transient gene delivery is one of the more attractive options. Gene delivery triumphs over protein delivery due to its longer effective window, increased stability, and high degree of adaptability due to the intrinsic nature of DNA. Genetic delivery to the wound bed can affect multiple generations of cells until the foreign genetic material is degraded internally, expelled extracellularly, or the transfected cells move away. At this point of reduced expression, it is ideal that the native wound healing processes will be able to take over the remaining healing process. Additionally, the cheaper, more stable genetic material can be adapted to code for any protein of interest thus making the therapeutic construct much more viable in a variety of applications or tissues.

Modes of DNA delivery can be categorized into viral and nonviral. Despite its less effectiveness at times, nonviral gene delivery is typically preferred as it avoids the potential of viral genetic integration or to provide a safer method[9]. Naked DNA delivery has several disadvantages including: requiring large amounts of DNA, often resulting in poor transfection rates due to extracellular degradation, and the surviving DNA usually has poor uptake by cells or can even illicit an immune reaction via inclusion foreign genetic motifs in the plasmid[9]. Condensing DNA into nonviral nanoparticles not only protects the genetic material but also enhances DNA uptake[8, 10-14]. Cationic lipids (e.g. Lipofectamine®) or cationic polymers (e.g. poly-ethylenimine (PEI)) are often used to create these nanoparticles[7-9]. Furthermore, the

enhanced efficacy of transfection of the DNA polyplexes requires less overall DNA loading into the hydrogel [8, 9].

Considering the colloidal nature of these polyplexes, it is unsurprising that higher concentrations lead to their aggregation[11, 15]. Aggregation is not ideal, leading to the apparent size of the polyplex increasing and the prevention of endocytic uptake by cells. To combat aggregation and permit higher levels of DNA loading, sucrose and low melting point agarose have been used to create caged nanoparticle encapsulation (CnE) of DNA polyplexes capable of a more even distribution within a gel[11, 15]. A more thorough description for CnE creation is discussed below. Polyplex diameter is typically greater than the usual mesh size of HA gels (mesh~20-100nm, polyplex~50-400 nm)[8, 11, 12, 16] thus assuring its immobilization.

The physical construct of the hydrogel itself has a great impact on its efficacy. Porous constructs have been shown to increase the levels of cell infiltration[17, 18]. The material discussed in the present work will be a mixture of nonporous and precast porous gels composed of the glycosaminoglycan hyaluronic acid (HA) functionalized with acrylamide groups to permit MMP degradable crosslinking. HA is naturally found throughout the body as an extracellular matrix (ECM) molecule. It has many functions ranging from regulating the inflammatory response to providing structure or organizing other aspects of the ECM, including collagen[19]. Ultimately, HA was chosen for its natural biocompatibility, proangiogenic properties, and the fact that HA oligomers promote endothelial activity leading to neovascularization[20-23].

Incorporating DNA/PEI polyplexes into porous HA constructs has been successful in transfecting cells *in vivo* [11, 24]; additionally, the partial degradation of gels loaded with CnE DNA have been shown to increase transfection rates[24]. However, this has never been replicated suggesting that the DNA availability and gel creation process could be more closely

examined for points of enhanced efficiency or optimization. For this reason, the present work describes a method to partially degrade HA constructs with hyaluronidase (HA-ase) to enhance polyplex diffusion through the gel, aid cell-mediated gel degradation, and cell infiltration of the gel. It is expected that partial degradation treatment should result in enhanced rates of transfection *in vitro* and provide more effective healing if transferred to an *in vivo* model.

While some successes have been observed with DNA loaded hydrogels, their consistency can be greatly improved. Huang et al. loaded 200ug condensed DNA (alternate form of CnE) into porous PLGA rigid scaffolds (termed 'sponge') and observed significant transfection rates *in vivo*[13, 25]; meanwhile, others have loaded nonporous, agarose gels (nonporous, injectable) with only 25ug of polylysine-DNA polyplexes (no sugar cryoprotection or lyophilization, therefore not a type of CnE) and observed significant transfection and healing effects *in vivo* as well[14]. The current field of local gene delivery via implantable construct appears to vary greatly in method but produce similar results. For this reason, another concern of this work is to evaluate various aspects of the process to make these therapeutic hydrogels, investigate various properties of the gels, and establish consistency in gels prior to advancing to *in vitro* work.

2 Materials and Methods

2.1 Hyaluronic acid modification

Hyaluronic acid (HA) was purchased from LifeCore or (Czech company) with molecular weights ranging from 40 kDa to 60 kDa. HA was functionalized with an acrylamide group to allow for click chemistry with the thiol group on either side of a peptide sequence recognized and cleaved by matrix-metalloproteinases (MMP) secreted by cells or administered by the researcher. The dithiol MMP peptide crosslinker sequence is GCRDGPQGIWGQDRCG and was purchased from GenScript.

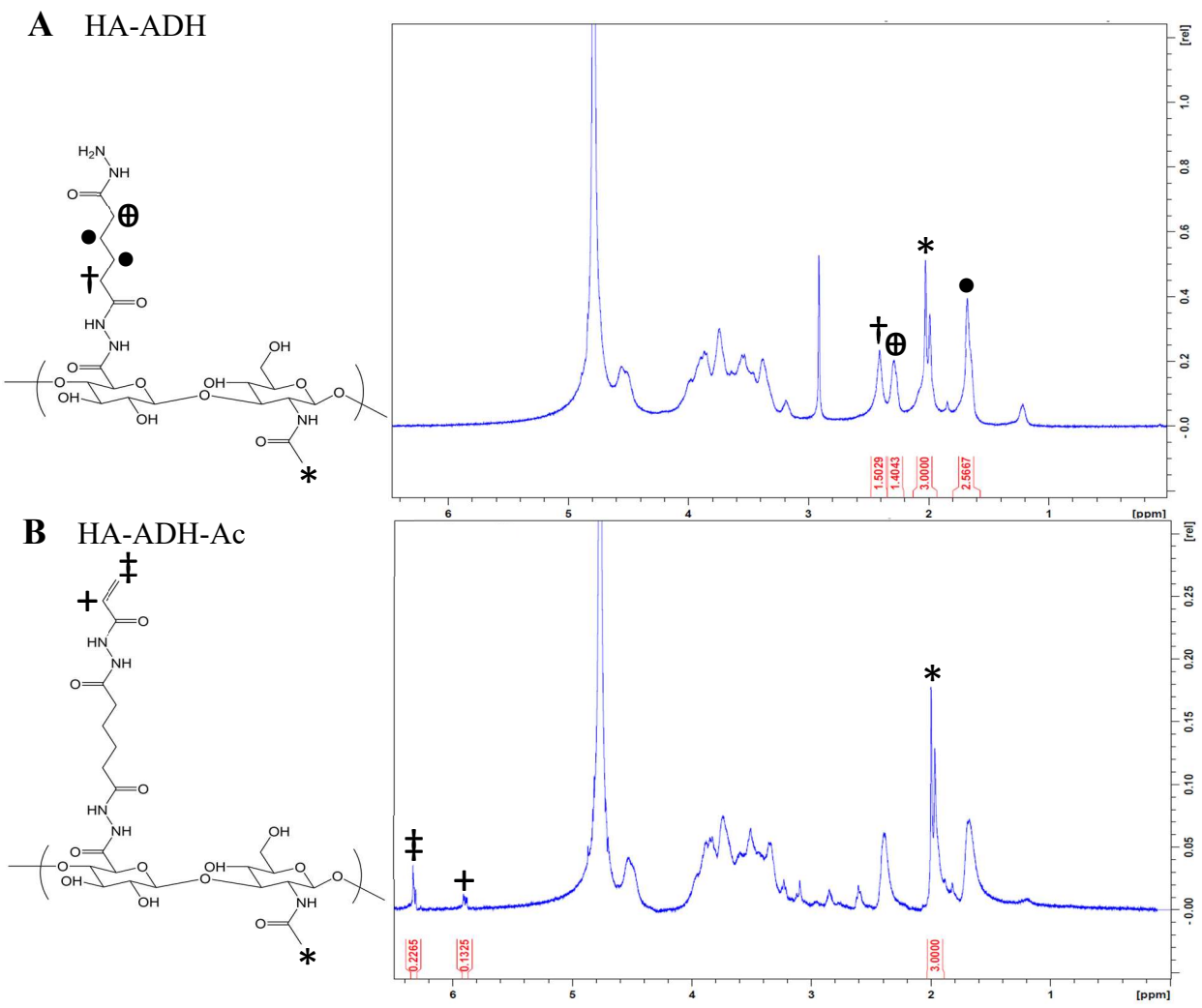

Figure 1: Determining HA functionalization with ADH and Ac via NMR. The reference hydrogen (*) used to scale integration peaks for measuring functionalization. **A:** ADH functionalization: $\frac{1.5029+\ .4043+2.5667}{8} \times 100\% = 68.42\%$, **B** Ac functionalization: $\frac{0.2265+\ .1325}{3} \times 100\% = 11.97\%$

The process of HA functionalization is as follows, also described in [11, 12, 16, 18, 24]. First, HA is dissolved in DI water to 5mg/mL. Add adipic dihydrazide (ADH) with a ratio of 40 mol ADH:1 mol HA residue and adjust the pH to 4.75. Additionally, add 1-ethyl-3-[3-dimethylaminopropyl] carbodiimide hydrochloride (EDC) with the ratio 3.95mol EDC:1mol HA residue to activate the carboxylic acid of the HA. Allow HA and ADH to react at room temperature overnight with stirring. Dialyze the HA-ADH against 100mM NaCl to pure DI water over 1 day and continue dialysis for an additional 4 days. Filter HA-ADH solution with a 0.22um

filter to remove precipitates and lyophilize for 3 to 4 days. Usually, ADH functionalization is measured at this point via NMR. Next, resuspend the HA-ADH to 5mg/mL in 10mM 4-(2-hydroxyethyl)-1-piperazineethanesulfonic acid (HEPES), 150mM NaCl, 10mM ethylenediaminetetraacetic acid (EDTA) at pH 7.4 and allow to mix. Add N-hydroxysuccinimide-acrylamide (NHS-Ac) with the ratio 5mol NHS-Ac:1mol HA residue. pH will likely drop; maintain the pH at 6 and allow HA-ADH to react with NHS-Ac overnight with stirring. Finally, filter HA-ADH-Ac final product with 0.22um filter and lyophilize for 3 to 4 days. The dry product can be stored at -20℃ until used.

Measurement of HA functionalization with ADH and Ac was measured by NMR (400uL of 10mg/mL HA-ADH-Ac in D2O) as shown in Figure 1. HA-ADH functionalization measured after the first lyophilization step.

2.2 CnE DNA Polyplex Creation

Throughout the present work two different CnE DNA polyplexes were used. Both types of polyplexes utilize PEI, one linear PEI, the other JetPEI. Despite their subtle differences, they perform similarly as the ratio of nitrogen on PEI to phosphate on the DNA remained constant at 7 N:P. Briefly, the desired amount of DNA and according amount of PEI/JetPEI are separately diluted in DI water. DNA is diluted to 0.0606 ug/uL, PEI/JetPEI is diluted to 0.204 ug/uL. Add 350mg/mL sucrose solution to diluted PEI/JetPEI; add 1uL sucrose solution/ug of DNA. Add sucrose and PEI/JetPEI solution to diluted DNA, vortex briefly and allow the formation of polyplexes at room temperature for 15 minutes. Add low melting point agarose (0.67 mg/mL) to the polyplex solution (15 uL agarose stock/ug DNA); immediately vortex for maximum 10

seconds and quickly freeze in liquid nitrogen for 5+ minutes. Lyophilize frozen CnE polyplexes and store at -20℃ until use[11, 15].

2.3 PMMA microsphere mold creation for porous gels

Molds are 8mm in diameter and contain 55mg of polymethylmethacrylate (PMMA) microspheres (either 53-63um or 93-106um diameter). PMMA microspheres are initially suspended in a solution of 70% ethanol and 1% acetone (0.1444mg/mL) prior to adding to circular wells; ethanol facilitates evaporation while the acetone chemically starts the sintering process. After adding suspended PMMA to wells (constructed of PDMS on glass), PMMA molds are dried for 45 min at 37℃ and followed by 14-18 hours of sintering at 100℃ (overnight). Gel solution perfused into the mold by two rounds of centrifugation at 700g for 5 minutes at 4℃ with a 180o rotation between spins. Gels are ensured to be 1mm in height by using a razor to slice the top off gels using a 1mm Teflon spacer. PMMA molds are dissolved by pure acetone bath over 48-72 hours with 2-3 changes in acetone per day.[18] Nonporous gels formed by sandwiching gel solution between two Sigmacoted glass slides with 1mm Teflon spacer.

2.4 Gel Formation

Gels had different compositions depending on their application. The basic gel contained HA-ADH-Ac and MMP crosslinker dissolved in 0.3M triethanolamine (TEOA) buffer at pH 8[11, 12, 16, 18, 24]; after the combination of precursor solution and crosslinker the gel forms over 30 minutes at 37℃ in a humid incubator. Lyophilized crosslinker was dissolved in a solution of 0.3M TEOA and 12.5mM Tris(2-Carboxyethyl) Phosphine Hydrochloride (TCEP) to

0.05 mg/uL; TCEP is included to prevent dimerization among crosslinker molecules prior to addition to the gel precursor solution. The amount of crosslinker to include in the precursor solution was determined by an r ratio defined as the number of thiols in the crosslinker to the number of HA chains; this work uses r ratio of 14 or 16. In general, all volumes going into the gel precursor solution (i.e. crosslinker, dye, etc.) are calculated and used to subtract from the final gel volume to provide the initial dissolving volume for HA-ADH-Ac and maintain the final volume; this ultimately ensures that the final gel product is of the desired wt%.

For gels that are fluorescently labeled either to track degradation or for imaging purposes, use 2.5*10^-2 uL dye/uL total gel volume. This ratio was empirically determined and provide adequate dyeing while also being a large enough volume to avoid pipetting inaccuracies that might disrupt HA wt% calculations. Gels were dyed with Alexa Fluor 647 N-Hydroxysuccinimide (AF647-NHS) or Atto 488-NHS; these molecules react with the primary amine on open HA-ADH groups as only a small fraction of HA-ADH residues are occupied by acrylamide groups.

Where gels were planned to have contact with cells, gels were functionalized with cell adhesion peptide, RGD (GCGYG**RGD**SPG) purchased from GenScript. Clustering of RGD is found to be more effective for cell adhesion[26, 27]; this work exclusively uses a clustering ratio of 1.17 RGD/HA chain. Add appropriate amount of HA-ADH-Ac (0.08mg/uL) to lyophilized RGD peptide aliquot and allow to react for 25 minutes at 37℃. Combine HA-ADH-Ac-RGD to get final RGD concentration of 100uM and balance amount of HA-ADH-Ac to make the gel precursor solution of the desired weight percent[4, 24].

All gels swelled and stored in PBS pH 7.4, 1% penicillin/streptomycin (P/S) at 4℃ for at least 12 hours before use.

2.5 Rheology

Rheological measurements taken with Anton Paar M301's 8mm diameter parallel plates. Gels are cut to the proper diameter by 8mm biopsy punches. Amplitude sweeps were conducted from x to y strain and stress to determine the appropriate range for frequency sweeps used to measure the storage moduli of future gels. At times, the storage modulus data collected at higher frequencies of the standard frequency sweeps deviate from the stable storage modulus regime and indicate shear thinning attributes; when analyzing storage modulus data, extreme frequencies are omitted.

2.6 Void Fraction

Void fractions of porous gels were determined via fluorescent image analysis of z stacks collected from the Nikon Ti Eclipse Confocal microscope. Given the porous nature of the gels (and the pore shape) laser diffraction was a limiting factor in the maximum imaging depth achievable; therefore, z stacks were usually ~100um tall with 5-10um between slices. Z stack brightness or contrast was not adjusted prior to analysis. Furthermore, porous gels were placed into a bath containing 2000kDa FITC-Dextran to obscure fluorescence not in the focus plane.

Analysis was completed with a custom MATLAB script or by IMARIS software. The MATLAB script is below. The script does contain some image enhancement; however, the same general enhancement is performed on all z stacks. Furthermore, a custom de-speckle script is included below and works by examining the surrounding pixels (creating 3px X 3px analysis box) and if there are greater than 7 surrounding pixels with signal, the pixel in question (center pixel) is determined to be significant and is filled as well. Ultimately, the inclusion of the custom noise reduction script did little to affect any void fraction results.

```
% Calculate Void Fraction of precast porous gels
```

```
close all
clear
'Where are your z stack files located?'
imagefiles=uigetdir([]); %Select folder containing zstack files

'Where would you like to save the initial analysis?'
savelocation=uigetdir([]); % select save location

imname=input('What is the base filename? (Ex. if filename is gel_001z1.tif, type
"gel_001z")','s');
N=input('How many images in this z stack?'); %number of images in z stack
IMAGES=cell(1,N);

zhigh=input('What is largest z value?');
zlow=input('What is smallest z value?');


%%
for k=1:N
   if k<10
   suffix=sprintf('0%d.tif',k);
   else
   suffix=sprintf('%d.tif',k);
   end
   tifFilename=strcat(imname,suffix);
   fullFilename=fullfile(imagefiles,tifFilename);
   if exist(fullFilename,'file')
       imageData=imread(fullFilename);
   else
       warningMessage=sprintf('Warning: image file does not exist:\n%s',fullFilename);
       uiwait(warndlg(warningMessage));
   end
image_o=(imageData); %may need to use rgb2gray if color image
image_adj = imadjust(image_o); %Image enhancement for greyscale


%%
sizeim=size(image_o);

%take off 5% of image on all four sides - edges are inaccurate
sizey=sizeim(1)-round(0.1*sizeim(1));
sizex=sizeim(2)-round(0.1*sizeim(2));
croplimy=round((sizeim(1)-sizey)/2);
croplimx=round((sizeim(1)-sizey)/2);
image_crop(:,:)=image_o(croplimy:sizey+croplimy-1,croplimx:sizex+croplimx-1);


threshold=multithresh(image_crop,2);


%%

image_gel=zeros(sizey,sizex);
image_void=zeros(sizey,sizex);
for i=1:sizey
    for j=1:sizex
        if image_o(i+round(0.05*sizeim(1)),j+round(0.05*sizeim(2)))<threshold
            image_void(i,j)=1;
        else
            image_gel(i,j)=50;
        end
    end
```

```
end

image_gel_nonoise=image_gel;
image_void_nonoise=image_void;

% Noise Correction - DeSpeckle
for i=2:sizey-1
    for j=2:sizex-1
        box=image_gel(i-1:i+1,j-1:j+1);
        numnonzero=nnz(box);
        if numnonzero>=7
            image_gel_nonoise(i,j)=50;
            image_void_nonoise(i,j)=0;
        elseif numnonzero<=3
            image_gel_nonoise(i,j)=0;
            image_void_nonoise(i,j)=1;
        end
    end
end

image_gel_fill=image_gel_nonoise;
image_void_fill=image_void_nonoise;


%%

image_invert=imcomplement(image_o(round(0.05*sizeim(1)):round(0.05*sizeim(1))+sizey-
1,round(0.05*sizeim(2)):round(0.05*sizeim(2))+sizex-1));
image_contrast=histeq(image_invert);
figure;
imshow(image_contrast)
hold on
red=cat(3, ones(size(image_contrast)),
zeros(size(image_contrast)),zeros(size(image_contrast)));
h=imshow(red);
set(h,'AlphaData', image_gel_fill);



folder = savelocation;
baseFileName = strcat(imname,sprintf('overlay_%d.fig', k));
fullFileName = fullfile(folder, baseFileName);
saveas(figure(1),fullFileName);

close


%% Calculating volume of void

deltaz=zhigh-zlow;

dz=deltaz/N;

vol_void_px=zeros(sizey,sizex);
vol_void_px_nonoise=zeros(sizey,sizex);

for i=1:sizey
    for j=1:sizex
        vol_void_px(i,j)=image_void(i,j)*dz;
        vol_void_px_nonoise(i,j)=image_void_fill(i,j)*dz;
    end
end
```

```
vol_void=sum(sum(vol_void_px));
vol_void_nonoise=sum(sum(vol_void_px_nonoise));
vol_total=sizey*sizex*dz;

void_frac=vol_void/vol_total;
void_frac_nonoise=vol_void_nonoise/vol_total;

OutputName = strcat(imname,sprintf('im%d',k));
save([fullfile(savelocation,OutputName) '.mat']);


end

close all
clear


string('What is the location of the initial or secondary analysis?')
source_dir = uigetdir([]); %Select folder containing initial analysis files

matfiles = dir([source_dir, '\*.mat']);
numfile=length(matfiles);

imname=input('What is the base filename? (Ex. if filename is gel_001z1.tif, type
"gel_001z")','s');

voidfracs=zeros(numfile,1);
for i=1:numfile
    suffix=sprintf('im%d.mat',i);
    basefile=strcat(imname,suffix);
    folder=source_dir;

vv_temp=load(fullfile(folder,basefile),'vol_void','deltaz','sizeim','sizey','sizex','v
ol_void_nonoise');
    voidvols(i,1)=vv_temp.vol_void_nonoise;
end

Dz=vv_temp.deltaz;
sizey=vv_temp.sizey;
sizex=vv_temp.sizex;
VoidFract_ave=sum(voidvols)/(sizey*sizex*Dz) %both volumes calculated by
pixel^2*differential height
```

When importing a z stack into IMARIS, the software will naturally fill in signal between z slices to create a 3D image. IMARIS analysis was completed by using the create object function that uses the fluorescence signal and k-means thresholding to create a solid object to mimic the solid gel. IMARIS is then able to provide much data on the rendered object like surface area and volume. The gel volume is subtracted from the total volume of the right rectangular prism to arrive at the void volume where the void fraction can be easily calculated. The settings used are: 1um smoothing factor and all surfaces “seen” are used for volume

calculations. Additionally, 5% of each end of the x and y axis is cropped out of the IMARIS analysis as fluorescence signal capture by the microscope camera is more irregular near the edges of the image.

2.7 Cell seeding – Centrifugation

Seeding cells into a porous gel was more difficult than originally expected and many techniques were attempted in order to provide the most thorough and uniform distribution possible; pore shape and size was not considered in this work as in [28]. Murine mesenchymal stem cells type D1 were used throughout this work and were purchased from ATCC. Cells were cultured and/or handled in modified DMEM media composed of DMEM+glucose, 10% Fetal Bovine Serum (FBS), 1% P/S unless otherwise stated and allowed to grow at 37℃ and 5% CO2, RH=95%. Porous gels, 8mm diameter, were placed into a well of a 96-well plate with 200 uL cell suspension (1000 cells/uL in modified DMEM) on top prior to centrifugation in a bucket centrifuge at various g's for 2 rounds of 5 minute spins with a 180o rotation between rounds. After centrifugation, cells were allowed to adhere to the gels for 30 minutes at 37℃. Gels were then moved to a fresh 48-well plate with new media for 4 hours to ensure adherence before fixing the cells with 4% paraformaldehyde in PBS for 15 minutes at room temperature or overnight at 4℃.

2.8 Cell seeding – Flicking

Seeding by flicking was accomplished by incubating gels in 500 uL of the same cell suspension as previously described (1000 cells/uL in modified DMEM) in a 1.5mL tube at 37℃ for 3 hours. Every 30 minutes the tubes were flicked and generally agitated to make sure the cells

were adequately suspended. After the 3 hours, gels were moved to a fresh 48-well plate with new media for 4 hours to ensure adherence before fixing the cells with 4% paraformaldehyde in PBS for 15 minutes at room temperature or overnight at 4°C.

2.9 Cell seeding – Syringe pump

Seeding by microfluidics was accomplished by sandwiching gels between 2 slabs of PDMS, diagram in Figure 2. The top slab has a 1mm height by 8mm diameter well to accommodate the gel without squishing it. There is a 1mm hole in the center of the circle well to allow the insertion of the microfluidic tube (20 gauge) that will deliver the cell suspension fluid to one side of the gel. Two additional holes are on either side (about 1.5 cm from the center punch) to allow the escape of the cell suspension after passing through the gel. The bottom PDMS slab is patterned with a series of parallel microfluidic channels that allows the cell suspension fluid to travel between PDMS slabs to reach the 2 flanking escape ports. Finally, the 2 PDMS slabs (with the gel loaded) were stably sandwiched together with a custom designed, hand-screw tightened, custom, 3D printed clamp (design available upon request).

500uL of cell suspension fluid (various cell densities) was loaded into a 1mL syringe with a 20-gauge needle tip. With the system all connected with microfluidic tubing, the syringe plunger is then depressed by hand very slowly over the next 30 seconds, sometimes pausing for 10-15 seconds or gently pulling back slightly on the plunger to prevent any potential cell build up on inter-pore connections. After all 500uL of the cell suspension fluid passes through the gel (but no air), the cells were allowed 30 minutes for cells to adhere before moving the gels to a fresh 48-well plate. After 4 hours of incubation with fresh media, cells were fixed with 4% paraformaldehyde in PBS for 15 minutes at room temperature or overnight at 4°C.

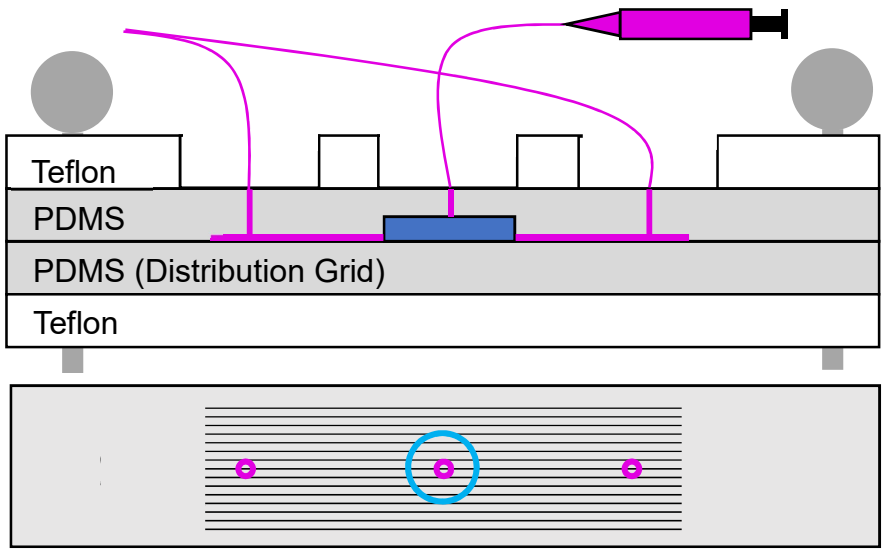

Figure 2: Schematic for the syringe pump system. Not to scale. **A**: side view portraying the different layers. **B**: top view of the bottom PDMS slab (Distribution grid), small circles indicate location of cell + media input/output, large circle indicates location of gel.

2.10 Cell seeding – Needle injection

Similar to the microfluidic setup, a 1mL syringe is loaded with 500 uL of cell suspension fluid; however, the syringe tip is replaced with a sharp 30-guage. Slowly depress the syringe plunger similarly to the microfluidic system. Administer cells to a variety of spots in the gel. Finally, the cells were allowed 30 minutes for cells to adhere before moving the gels to a fresh 48-well plate. After 4 hours of incubation with fresh media, cells were fixed with 4% paraformaldehyde in PBS for 15 minutes at room temperature or overnight at 4°C.

2.11 Evaluating cell seeding – Gelatin Embedding for cryo-sectioning

Considering the difficulties of 3D imaging porous gels as previously mentioned, seeded gels were embedded in gelatin, frozen to -20°C, and sectioned to provide insight on the center of the gels. Briefly, gelatin type A is dissolved in 15wt% sucrose in PBS to 10wt% gelatin; heating the solution to 60°C is likely required to fully dissolve the gelatin. Gels and gelatin solution are placed into an embedding cube and slowed to equilibrate at 37°C for at least 1 hour before

putting into the embedding cube in a 4℃ fridge to harden. Be sure to position the gel according to the desired angle; typically, gels were sectioned parallel to their circular face.

After the gelatin cube containing gel have hardened, remove them from the embedding cube and place in 15wt% sucrose in PBS for at least 4 hours. Then place gelatin cubes in 30wt% sucrose in PBS overnight. After removing the gelatin cubes from the sucrose solution, freeze the cubes unidirectionally by placing the cutting face down on a block of dry ice (aluminum foil and parafilm between gelatin cube and dry ice). After freezing, gelatin cubes should be stored at -20℃ until used.

Sectioning was completed by the Leica NX50 cryostat. Sections were 100um, collected at ~18℃ and placed on glass slides.

2.12 Degradation

Gels were degraded in solutions containing either hyaluronidase (HA-ase) or collagenase type 1 (Col1) purchased from Sigma Aldrich and Fisher Scientific, respectively. Enzymes were dissolved in PBS to desired concentration (in U/mL); HA-ase optimal pH range is 4.25-6, Col1 optimal pH is 6.3-8.8 from Sigma-Aldrich product specification sheets. Degradation took place in 24-well plates with wells containing gels and 500uL of degradation solution. Gel degradation was tracked by measuring the amount of AF647 fluorescence present in the supernatant collected every hour. 200 uL of the 500 uL collected are placed into a 96-well plate and measured by a plate reader (Tecan Spark); either keep the laser intensity and gain consistent between measurements or simply analyze all time points at the same time to ensure similar excitation and emission conditions. Raw concentration of AF647 was not calculated, rather hourly relative fluorescent units (RFU's) were collected and used to calculate a total RFU. The total RFU was

used to determine how much each gel was degraded in each hour. In the case where gels needed to be partially degraded and a total RFU cannot be determined, a dummy gel subject to identical conditions was used to measure the total RFUs so the degree of partial degradation could be calculated. However, in 2 particular gel sets, a dummy gel was not able to be created due to lack of material or the precursor solution was too viscous to utilize the entire volume of the gel created. This is not ideal, but I am confident in reported partial degradation percentages for these sets due to the very consistent degradation profiles, shown below.

2.13 Mesh Size – Network theory

The equation used to determine mesh size via network theory is as follows: $\xi = \sqrt[3]{\frac{6}{\pi \rho_x N_a}}$ with $\rho_x = \frac{G' \sqrt[3]{Q}}{RT}$ where ξ is mesh size, ρx is crosslinking density provided by rubber elasticity theory, G' is storage modulus, Q is swelling ratio $\left(\frac{mass_{wet}}{mass_{dry}}\right)$, R is the ideal gas constant, and T is temperature[29-32]. The storage modulus is measured according to previously described rheological procedure. The wet mass is measured by placing the hydrated gel on a glass slide and lightly dabbing with a Kimwipe to wipe away any excess fluid. Gels were dried by placing the slide-mounted gels into a lyophilization chamber and allowed to dry overnight.

2.14 Mesh Size – Fluorescence Recovery After Photobleaching (FRAPs)

FRAPs is a very common method to determine the diffusivity of solutes in a medium[33-36]. The measured diffusivity can then be used to determine the mesh size with the following equation: $\frac{D_{gel}}{D_{water}} = \left(1 - \frac{r_s}{\xi}\right) \exp\left(-Y\left(\frac{\varphi}{1-\varphi}\right)\right)$ [37]. Where D refers to solute diffusivity in gel and

water, r_s is the solute's Stoke radius, φ is the polymer volume fraction, Y is the ratio of the critical volume required for a successful translational movement of the solute to the average free volume per liquid molecule (~1), and ξ is the mesh size.

Gels loaded with 70kDa FITC-Dextran; 1uL of 100 mg/mL. Similar to dyeing protocol, 1uL of fluorescent material used to avoid smaller volume inaccuracies. Gels allowed to swell for at least 12 hours before placing them between glass sides with a 1mm Teflon spacer to maintain gel hydration while monitoring the fluorescence recovery. Photobleaching accomplished with 100% power 488 laser performing 20 sweeps across a circular region of interest (ROI). Sweep speed was ½ diameter/sec. Recovery was monitored over the next 220 minutes.

FRAPs recovery was analyzed with the free software, Fiji (is just ImageJ). The .nd2 files generated by the Nikon Confocal Fluorescent microscope were imported to Fiji with the Bio-Formats plugin Image; contrast or brightness was not altered due to the nature of this experiment. For porous gels, a mask of the porous network was generated by binarizing the preliminary images (prior to photobleaching). The mask was then used to subtract the area known to be void space to allow accurate tracking of the dextran within the gel and avoid fluorescent signal of FITC-Dextran that has diffused out of the gel and into pores.

To reduce the effects of dextran diffusion in the third dimension, the fluorescence data within the ROI was normalized external fluorescence signal. This relative fluorescence recovery is then fit to the FRAPs recovery curve: $I(t) = I_{max}(1 - e^{Kt})$ [36]. Where I is fluorescence intensity, K is the exponential factor, t is time, and I_{max} is the intensity at long time. The fit provides a time of half recovery which is used in Soumpasis' equation for FRAPs recovery with a circular geometry: $D = 0.224 \left({w^2}/{t_{\frac{1}{2}}} \right)$ [35]. Where D is solute diffusivity, w is radius of photobleached ROI, and $t_{1/2}$ is the time of half recovery.

3 Results and Discussion

3.1 Rheology

As mentioned, one of the two metrics to analyze gel consistency was rheology, results in Figure 3. This figure shows how 3.5wt% gels appear to have more consistent storage moduli as time progresses over a year and stabilize at a G' slightly lower than 300Pa. It was decided to increase the weight percent of gels to 4.5% (from 3.5%) for a few reasons: 1. Stiffer gels are typically easier to handle and measure, 2. The rheometer requires a non-zero storage modulus to be accurate, thus starting at a higher G' will allow for the measurement of G' after partial degradation, 3. Human dermis has a G' that hovers around 400-600Pa [38] which is more regularly achievable by 4.5wt% rather than 3.5wt%.

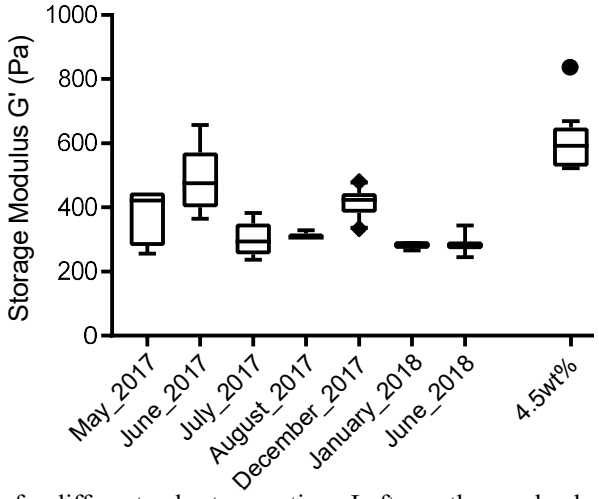

Figure 3: Rheology results for different gel sets over time. Left months are rheological results for 3.5wt% gels, a single 4.5wt% is included on the right for comparison.

3.2 Void Fraction

The second metric for consistency in gel creation was the void fraction. It is important to verify the geometric structure of the porous gels as surface characteristics (including rheometric aspects coincidentally) can influence the activity of those cells directly interacting with said surface[39]. A summary of the void fraction analysis can be found in Figure 4; which, similarly to the rheometric data displays consistency over time.

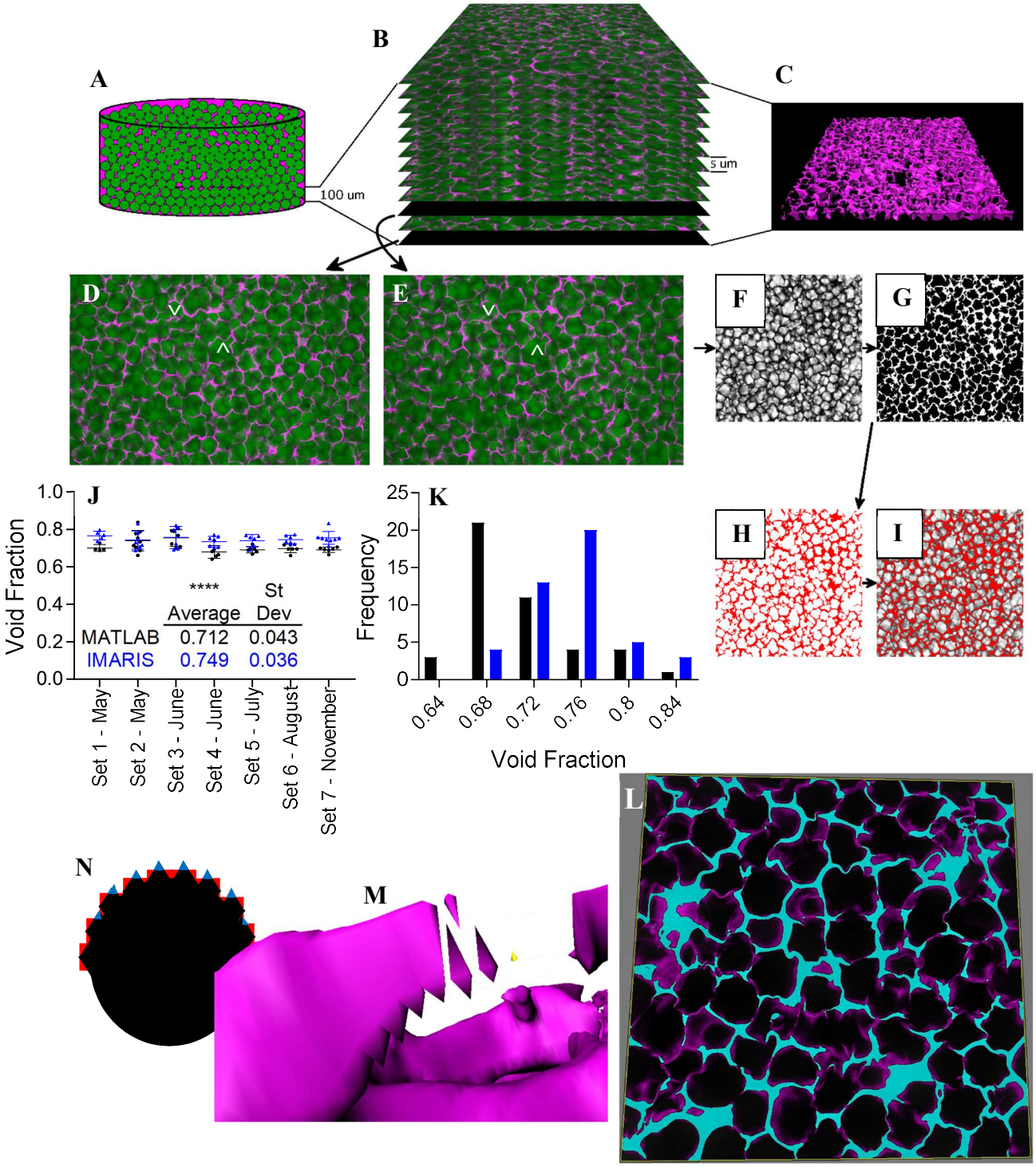

Figure 4: Void fraction results. **A**: Digital representation of the PMMA mold (green spheres) and gel (pink) **B**: Example z-stack of a precast porous gel. Gel is pink, green is void. **C**: 3D rendering of the gel by IMARIS **D, E**: Example slices of a z-stack, carrots point to two spots where an alternate "z" can be seen **F, G, H, I**: progression of the MATLAB analysis; F greyscale the image, G invert black and white intensity, H develop mask to calculate void fraction, I simply overlays the mask on the greyscale image to allow easy comparison **J**: Void fraction data separated by sets over time, **** indicates significance by t test, $p<0.0001$ **J**: Histogram of MATLAB and IMARIS void fraction data **M**: Very zoomed section of IMARIS rendering, yellow voxel simply indicates center voxel for axis of rotation in IMARIS **N**: Artist interpretation of voxel shape and dimensions. Black represents agreement between MATLAB and IMARIS, red indicates MATLAB voxel shape, blue indicates IMARIS voxel shape **L**: A middle slice of a gel (dim magenta) with the IMARIS rendering overlay (teal) provides an example of IMARIS deconvolution.

Although consistency was the goal and it appears to be achieved, it is interesting to note the slight disagreement between the MATLAB and IMARIS analysis (Figure 4K). Now, there are quite a few factors that could influence this result. First, I would like to preface that the IMARIS software is immensely more sophisticated than the simple script introduced previously and without a doubt capable of a wide variety of different analysis and calculations. An example of this is the likely presence of a deconvolution step in its thresholding process; this would explain why IMARIS calculations typically yield larger void volumes as IMARIS 'sees' less gel after deconvolution. This deconvolution is not confirmed however, the use of purely automatic settings often resulted in unrealistically high void fractions nearing 0.9. For this reason, the threshold for determining gel presence was not consistent between analyses. It should not have to be stated how flawed this is from a scientific point of view.

Months were spent adjusting parameters in IMARIS including smoothing factor, background subtraction, and constant offsets from automatic results; however, no combination settings provided the consistency easily observed in the physical product and raw images. As such, the 3D rendering used to calculate void fraction is determined by manually setting the threshold and visually inspecting the rendering to evaluate accuracy. In an attempt to reduce bias, fellow graduate students (2-3) were consulted when setting the manual thresholding until a threshold could be agreed upon. Each IMARIS analysis is saved and is, of course, available upon request.

Secondly, IMARIS is able to import the raw .nd2 files provided by the microscope. This is important as this file type contains z data that IMARIS can use to accurately interpret signals that may not be in the same focus plane. MATLAB cannot do this. Instead, MATLAB would often mistake fluorescence signal not in the focus plane as real signal, thus leading to an

incorrect mask representing too much gel and ultimately resulting in a much lower void fraction. To combat MATLAB's overzealous recognition of fluorescence signal, porous gels were bathed in a solution containing 2000kDa FITC-Dextran prior to imaging. As mentioned previously, this helped to obscure signal not in the focus plane (Figure 4.D,E). Even though, the FITC-Dextran bath helped, it is quite possible that some signal from neighboring planes could contribute to the creation of the MATLAB gel mask leading to a lower void fraction.

Thirdly, the voxel is different between the two analysis methods. MATLAB uses a simple cube voxel with rigid dimensions equal to the pixel area by z stack differential height; meanwhile, IMARIS uses a stacked, 4-sided pyramid voxel. Even more, the IMARIS voxel appears to vary in size depending on the intensity of the signal present (Figure 4.M); another example of IMARIS sophistication. A 2D artist representation of how voxel shape can affect the apparent gel volume is shown in Figure 4.N. Given a curved shape (in this case a circle) and the exact same thresholding results, the MATLAB voxels appear to contain much more erroneous area than the IMARIS voxels indicating that MATLAB 'sees' more gel (and less void). Considering this effect is expanded to 3D in actual analyses, it is unsurprising that the two methods disagree in the way that they do.

Despite their differences, the results of void fraction resulting from both MATLAB and IMARIS analyses provides confidence in the consistency of gel creation. Additionally, the raw numerical results of 0.71 and 0.74 void fraction aligns directly with dense packing of monodisperse spheres, packing fraction 0.7405. The molds presented here, and gel created from them, do not exhibit the densest sphere packing possible; however, polydisperse spheres are able to pack to denser conformations more easily than monodisperse. From this, the average void fraction (MATLAB+IMARIS) of 0.725 is entirely reasonable.

3.3 Degradation Profiles

Precise control over degradation was crucial as other aspects of this work depend on the use and analysis of partially degraded gels. Results concerning degradation including its tracking and termination can be seen in Figure 5. Overall, gel degradation was very consistent and predictable. Figure 5.A's first 2 data points lying on top of each other indicates technical consistency; meanwhile, Figure 5.E exemplifies robustness among biological replicates (3 separate gel sets, 3 different days, 3 different degradation buffer creations). From these profiles, accurate partial degradation was achievable to within ~5% degradation. This accuracy is, again, displayed by Figure 5.A as 20% cumulative degradation was the desired degradation from the experimental design standpoint.

In controlling degradation, halting degradation is just as important as inducing it. Given HA-ase's enzymatic nature, it can be inhibited, denatured, or otherwise compromised to limit functionality or eliminate it entirely. Certain compounds like L-ascorbic palmitate and glycyrrhizin are shown to inhibit HA-ase activity[40, 41], but some of these inhibitors have been shown to inhibit other biological processes[42-45]. Instead, physical conditions were altered. Specifically, temperature was reduced, and various pH's were used in attempts to reversibly halt gel degradation by HA-ase. The results for replacing the warm (37oC) degradation solution with cold (4oC) PBS solutions of varying pH can be seen in Figure

4.A,C. Figure 5.A,C clearly indicate that cold solutions at lower pH (~5.25) reversibly inhibit gel degradation the best with a mere ~4% degradation over 24 hours. This is counter intuitive as the optimal pH for HA-ase function is pH 4.25-6. This is evidence of the importance of temperature to proper HA-ase function. This may also explain the slight

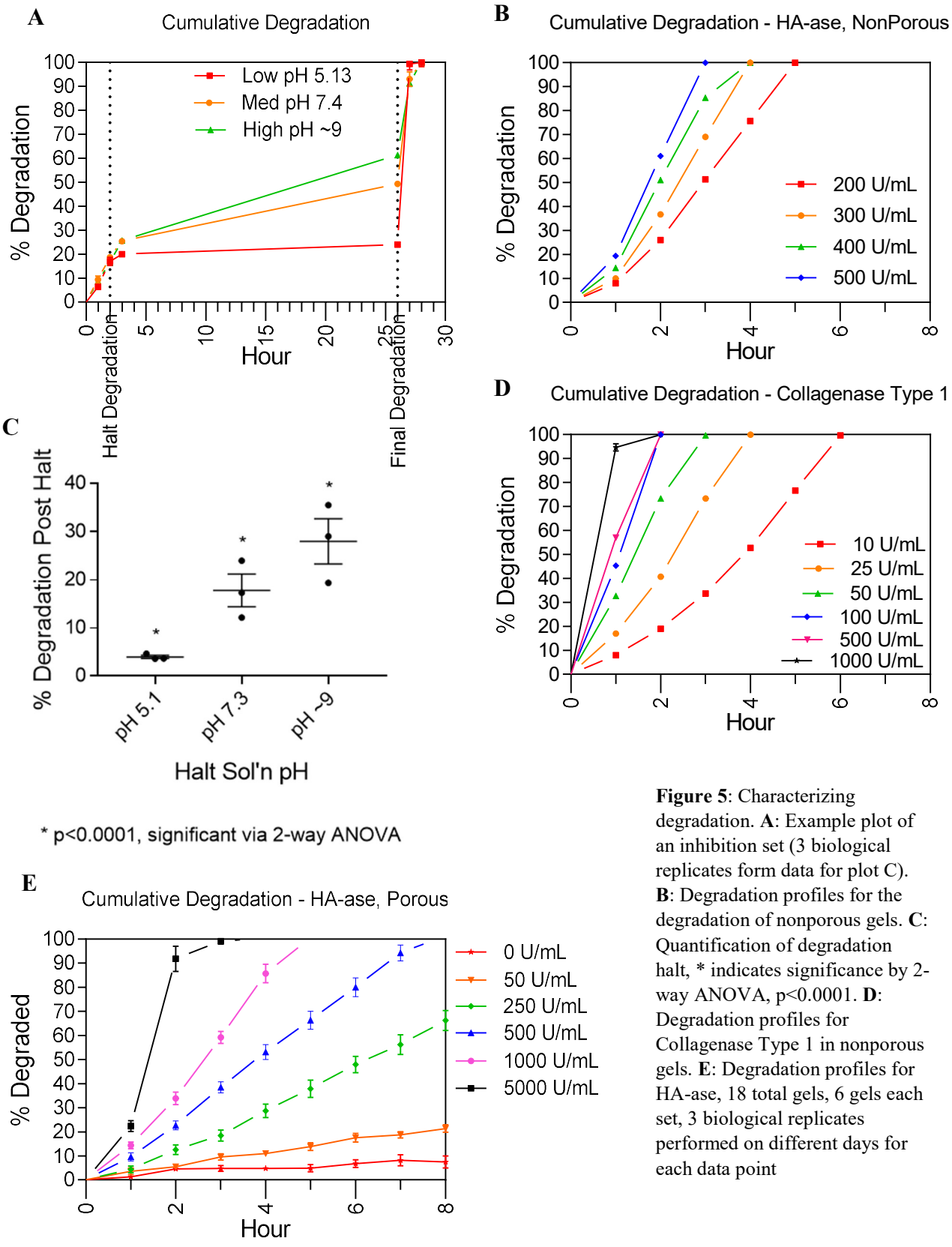

Figure 5: Characterizing degradation. **A**: Example plot of an inhibition set (3 biological replicates form data for plot C). **B**: Degradation profiles for the degradation of nonporous gels. **C**: Quantification of degradation halt, * indicates significance by 2-way ANOVA, $p<0.0001$. **D**: Degradation profiles for Collagenase Type 1 in nonporous gels. **E**: Degradation profiles for HA-ase, 18 total gels, 6 gels each set, 3 biological replicates performed on different days for each data point

degradation observed in the control degradation profile containing 0U/mL of HA-ase in Figure 5.E.

From Figure 5.A,C the gel appears to continue to degrade in higher pH conditions even though all 3 cases the HA-ase should be equally inactive by the universally lower temperature. Nonspecific degradation or release of labeled HA of the gel must be occurring, including possibilities like higher pH facilitating the physical expansion of the gel. Higher pH solutions containing more negatively charged hydroxide ions will infiltrate the mesh of the gel and considering HA's negatively charged nature, the backbones composing the gel may repel each other to permit the release of HA fragments previously degraded

3.4 CnE Distribution/Aggregation

Gels loaded with CnE DNA and Fresh PP DNA were imaged (Figure 6) to evaluate the distribution of DNA and verify that CnE DNA were indeed less prone to aggregation when compared to PP DNA. Clearly, Figure 6A,B show how CnE DNA is much more uniformly distributed throughout the porous gel. In fact, the porous structure of the gel can even be seen in the CnE DNA images due to its uniform distribution. The Fresh PP DNA did not distribute throughout the gel; though, this was expected. Instead of uniformly distributing in the gel, the PP DNA collected into dense particles, Figure 6.C,D.

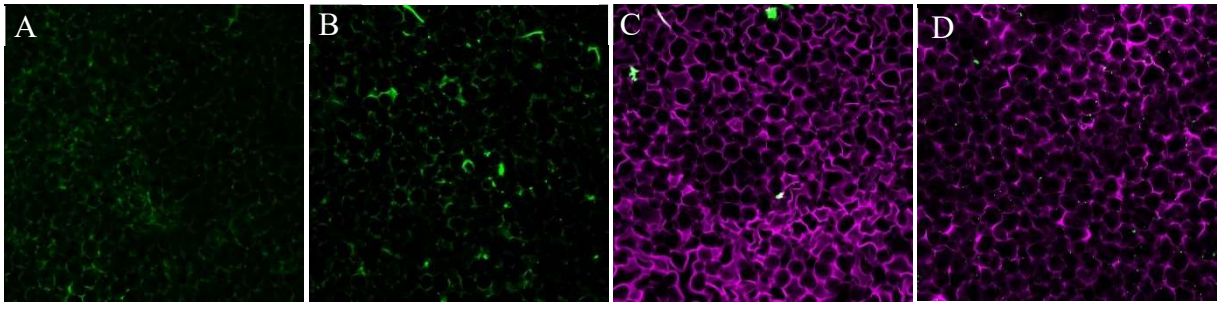

Figure 6: Visualization of polyplex distribution in porous gels. Pore diameter 90-110um. **A**: CnE loaded gel, 1.0 ug DNA/uL gel. **B**: CnE loaded gel, 0.25 ug DNA/uL gel. **C**: PP loaded gel, 1.0 ug DNA/uL gel. **D**: PP loaded gel, 0.1 ug DNA/uL gel. Gel in pink, polyplexes (CnE and PP) stained with sybr green post

3.5 Cell Seeding

Mentioned previously, cells were seeded in a variety of different ways as adequate cell presence is most certainly required for substantial transfection to occur. Seeding via centrifugation failed in every condition (images not shown). While centrifugation of cells is often used to force the migration of cells to the bottom of a tube, this migration is entirely due to gravitational forces and no actual fluid flow. The lack of flow in the seeding process meant that once the cells came in contact with the gel, they would get stuck similar a traditional filter. Consequently, the centrifugation of cells would generate a plaque of cells that would rest on top of the porous gel without actually penetrating the porous network.

Considering the failures of centrifugation, forcing flow through the gel was the next logical experiment. With fluid flow, entrained cells would be able to reach the deepest parts of the gel while also breaking up potential cell plaque buildup during the seeding process. From Figure 7, it appears abundantly clear that the syringe pump seeding method is superior. Figure 7 shows two different seeding sets (6 and 8) with different seeding conditions and methods of analysis which is not ideal but they both show similar trends.

Seed set 6 was completed using 1000 cell/uL solution with the analysis being the form of a z stack. As mentioned previously, imaging the gel deeper than 100 um can be difficult, yet we were able to capture cell nuclei presence to a depth of around 225 um as resolution was less important (this is why gel fluorescent channel not shown). Even from the histogram for cell location in seed set 6, the syringe pump seems to be better despite the cell density appearing to diminish rapidly at increasing depths into the gel. However, it is likely that laser intensity similarly rapidly decays with increasing gel depth which may explain such a dramatic drop.

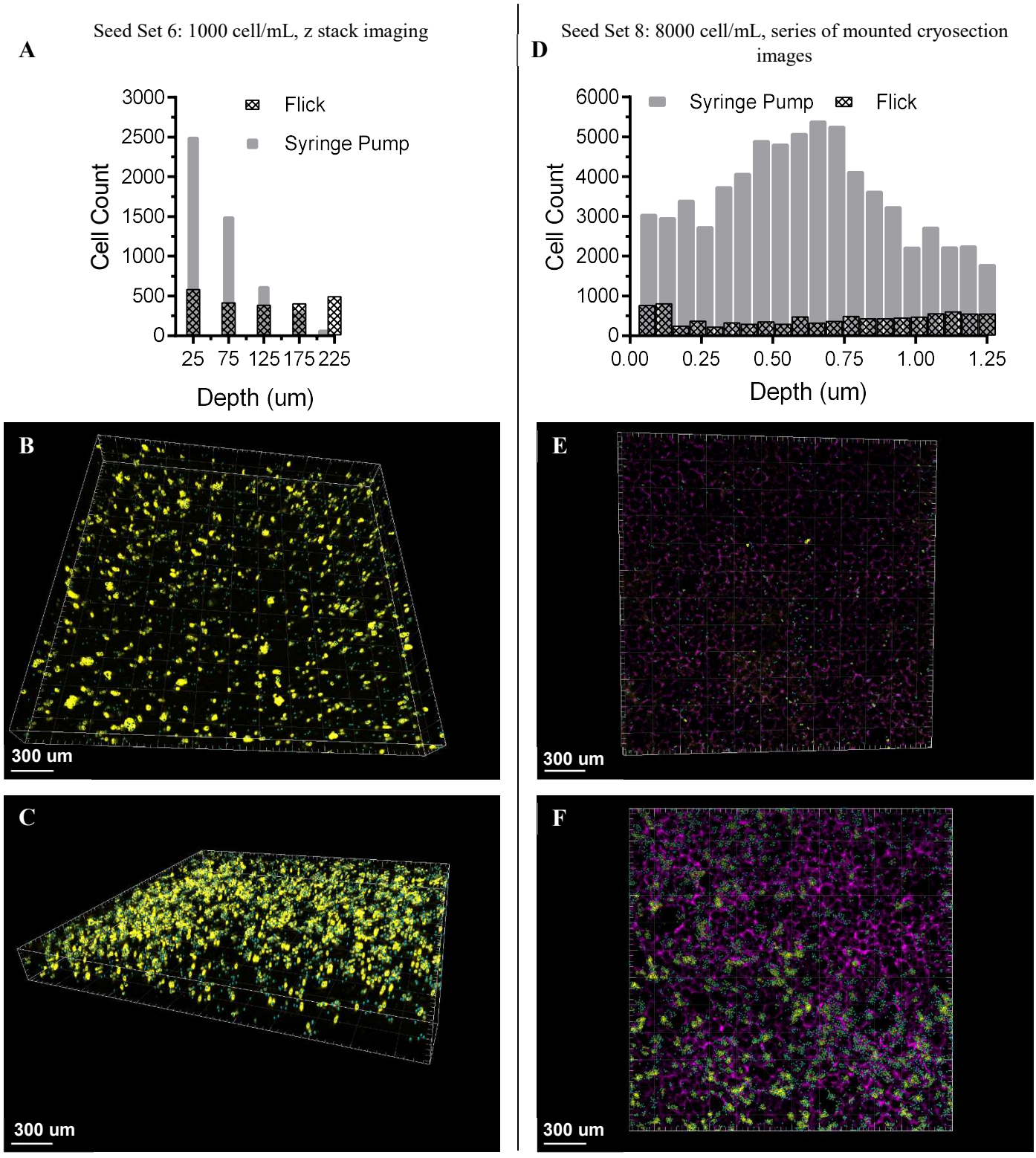

Figure 7: Cell seeding results. Left: Seed Set 6 experiment, 1000 cell/mL only imaged with a confocal z stack. Right: Seed Set 8 experiment, 8000 cell/mL seeded gels cryosectioned, mounted and imaged on the confocal microscope. A,D histogram of respective cell distribution data. B,E representative image of Flick method. C,F representative image of syringe pump method. Furthermore, E,F of Seed Set 8 taken from approximately half total height of gel. All scale bar 300 um. Colors: Gel is pink, Cell nucleus is yellow, IMARIS Cell Count is teal sphere.

Seed set 6 was completed using 1000 cell/uL solution with the analysis being the form of a z stack. As mentioned previously, imaging the gel deeper than 100 um can be difficult, yet we were able to capture cell nuclei presence to a depth of around 225 um as resolution was less important (this is why gel fluorescent channel not shown). Even from the histogram for cell location in seed set 6, the syringe pump seems to be better despite the cell density appearing to diminish rapidly at increasing depths into the gel. However, it is likely that laser intensity similarly rapidly decays with increasing gel depth which may explain such a dramatic drop.

Seed set 8, using 8000 cells/uL, clearly shows the dominance that the syringe pump has over the flicking method. Not only does the histogram in Figure 7.D have the syringe pump completely overshadowing the flick method, but the following representative images below also visually show the vast amount of cellular presence in the syringe seeding method. In future experiments the syringe method is almost exclusively used, though at a lower cell density (4000 or 6000 cell/uL). This is because Figure 7.F shows some pores completely filled with cells; this is not ideal either as the innermost cells may not receive the nutrients required to live or may use the nutrients for those cells that have actually transfected thus reducing the apparent transfection efficiency.

Seeding by needle injection (not shows as images are quite large) show similar seeding abilities to the syringe pump, but have lower cell counts near the edge of gels. This is most likely due to human error and not placing the needle tip near the edges of the gel.

3.6 Mesh Size

Mesh size can be measured in a variety of different ways and can produce several different results. As mentioned previously, here we present two common methods of measuring

mesh size: network theory and FRAPs. Figure 8.A,B shows how gel weight percent and r value influence mesh size. It is expected that an increase in either would decrease the mesh size either due to physical chain interactions or chemical linkages. Yet Figure 8.A indicates that only weight percent affects the mesh size of the gels; however, it could be argued that the range of r values examined was too narrow and that perhaps an r ratio of 40 or 50 may start to influence mesh sizes. Furthermore, Figure 8.A shows the agreement between network theory and FRAPs (also 4.5wt%).

Despite similar gel formulations, there is a statistical difference between the FRAP porous and nonporous gels. It could be that the acetone treatment used to dissolve the PMMA mold constricts the gel to a point where full swelling is no longer possible. Or the fact that the dextran must diffuse through small channels (pore walls) creates a bottleneck for traveling molecules. Finally, and perhaps the most likely, the dextran has much greater access to void space with a much lower restriction on free diffusion; if the FITC-dextran diffuses out of the porous gel and into the void, the amount of fluorescent decreases producing an artificially slower recovery and smaller mesh size.

Finally, Figure 8.C portrays how the mesh size of gels changes when partially degraded with HA-ase. Considering that partial degradation compromises the integrity of the gel backbone, it makes sense that partial degradation increases the mesh size.

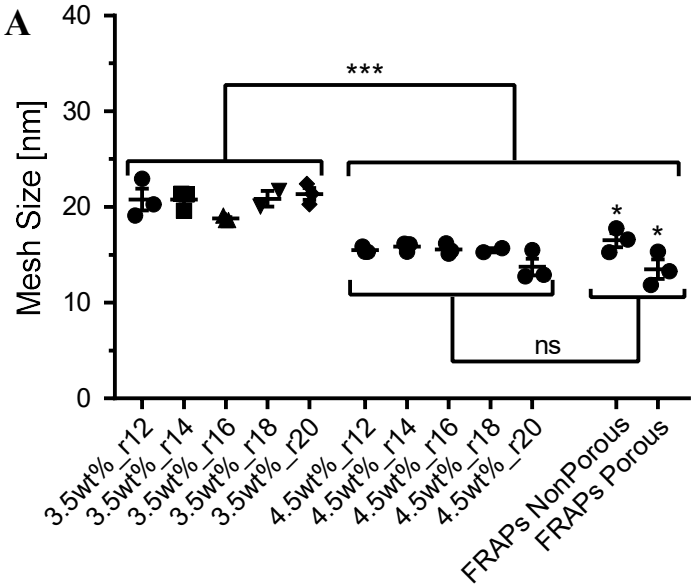

* Indicates significance by 1-way ANOVA,
* p value<0.05, *** p value≤0.0002

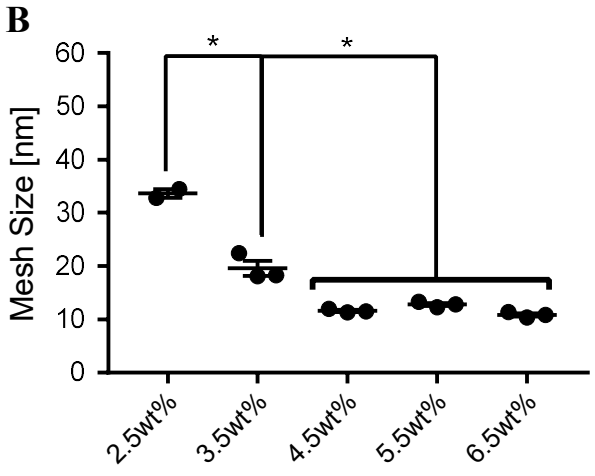

* Indicates significance by 1-way ANOVA, p<0.007

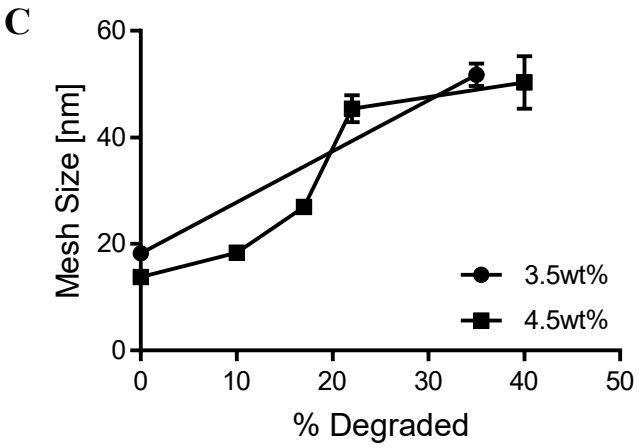

Figure 8: Mesh size summary. **A** shows how the r ratios affect mesh size and includes the FRAPs results. The FRAPs gels were 4.5wt% r16. **B** shows the mesh size for gels of varying wt% **C** shows the mesh size foe gels of varying partial degradation.

Figure 9 summarizes the FRAPs data including example images. The signal decrease from photobleaching is easily seen in the images and the signal profile. Additionally, the signal profile over time illustrates how the FITC-dextran diffuses over time and spatial positioning of

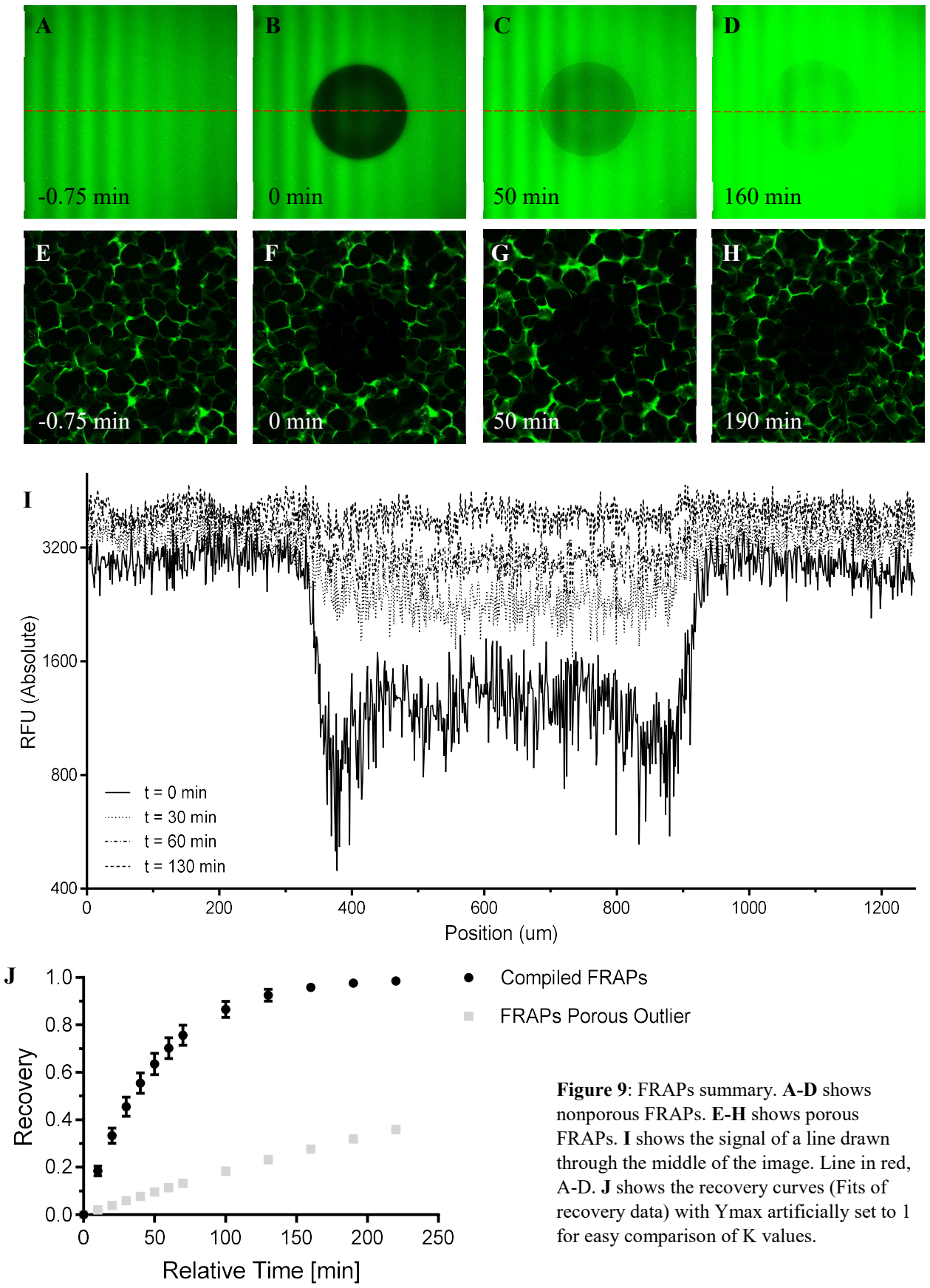

Figure 9: FRAPs summary. **A-D** shows nonporous FRAPs. **E-H** shows porous FRAPs. **I** shows the signal of a line drawn through the middle of the image. Line in red, A-D. **J** shows the recovery curves (Fits of recovery data) with Ymax artificially set to 1 for easy comparison of K values.

recovery. Finally, the traditional FRAPs recovery curve is included in Figure 9D. When examining the images for FRAPs recovery (Figure 9.E-H) the recovery is quite dim, so the resulting recovery curve based on raw experimental data is often quite low when compared to the nonporous FRAPs. To combat this, the preexponential factor, I_{max}, in the fit equation is set to equal 1 for all gels; while, the exponential coefficient, K, is specific to each FRAPs experiment. Figure 9.J compiles all FRAPs fitted recovery curves except for 1 outlying fit.

3.7 Transfection

To reiterate, the goal of all the characterization and technique development is to provide a platform for partial degradation of DNA loaded hydrogels producing higher rates of transfection *in vitro*. The results of two types of transfection are shown in Figure 10. The porous gel transfections (left) were completed with the flicking seeding method (1000 cells/uL) and produced negligible transfection; this is what spurred ideas for alternative seeding techniques like the syringe pump. Unfortunately, transfection experiments using the new seeding method (syringe pump) to seed cells onto gels were not conducted but are intended to be completed in the near future.

In the plot to the right, the nonporous gel partial degradation clearly has a beneficial effect on the rate of transfection. One of the concerns in the success of the nonporous partial degradation is that it is possible that the CnE DNA nanoparticles were leeching out of their hydrogel where they can transfect the other cells that may/may not be adhered to the bottom or walls (far away from the gel). Ideally, the cells would only grow and transfect on the gel; however, this idea of leeching DNA is not entirely detrimental if ever used in the field. The DNA leeching to surrounding areas of a wound site would still enhance the rate of wound healing by

similar pathways only the cells expressing the DNA are on the periphery rather than internal cells. It is possible, also, that peripheral expression enhances the rate of wound healing even more than if the sequestered internal cells had similar expression levels.

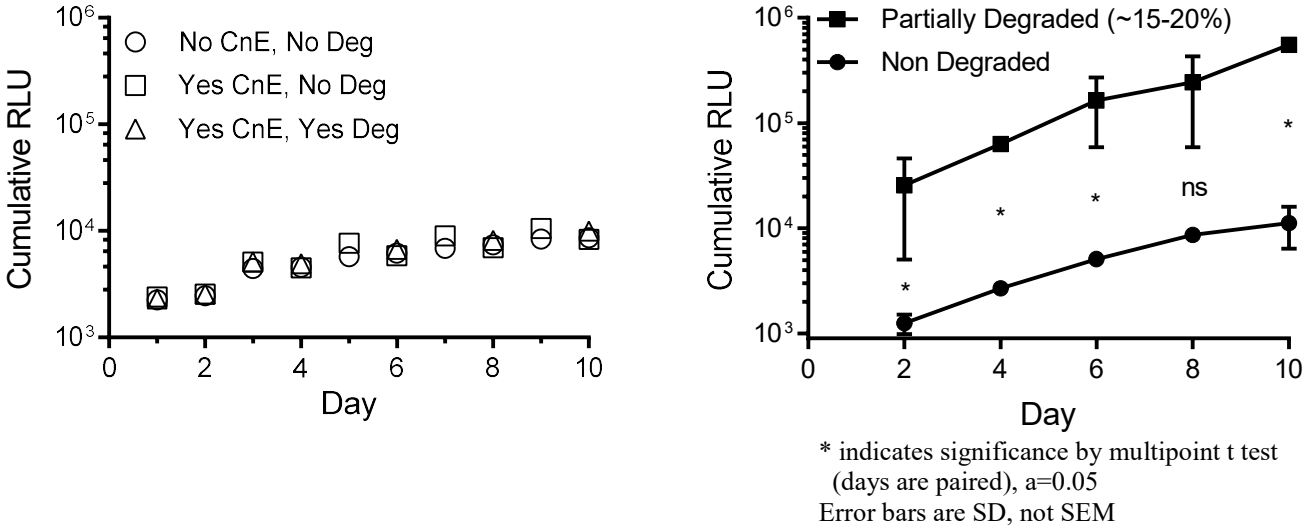

Figure 10: Transfection of cells by CnE loaded gels. Left plot portrays the transfection in porous gels, Deg implies partial degradation of ~30% (n=3); SEM error bars covered by data points. These gels were seeded using the highly ineffective flicking method. Right plot shows the transfection on cells on top of nonporous gels (n=2). These gels bathed in 1000 cell/uL and permitted to adhere for 30 minutes.

3.8 Cell Infiltration

In addition to enhancing transfection, it is desired that partial degradation facilitates cell infiltration of the gel itself. With decreased mesh integrity, it is likely that cell will more easily find a way to adhere more easily and even begin to grow into the gel; this is seen in Figure 11. The nondegraded gels in Figure 11A,B show an obvious plaque-like macrostructure that appears to simply sit on top of the gel, perhaps degrading the gel as a singular unit and digging a 'well'. The partially degraded gel in Figure 11C,D show how individual cells are able to be more independent and form 'fingers' that stretch deeper into the nonporous gel. This is more ideal as faster cell infiltration will likely reduce any foreign body response, reduce scar formation, and increase availability of the loaded DNA.

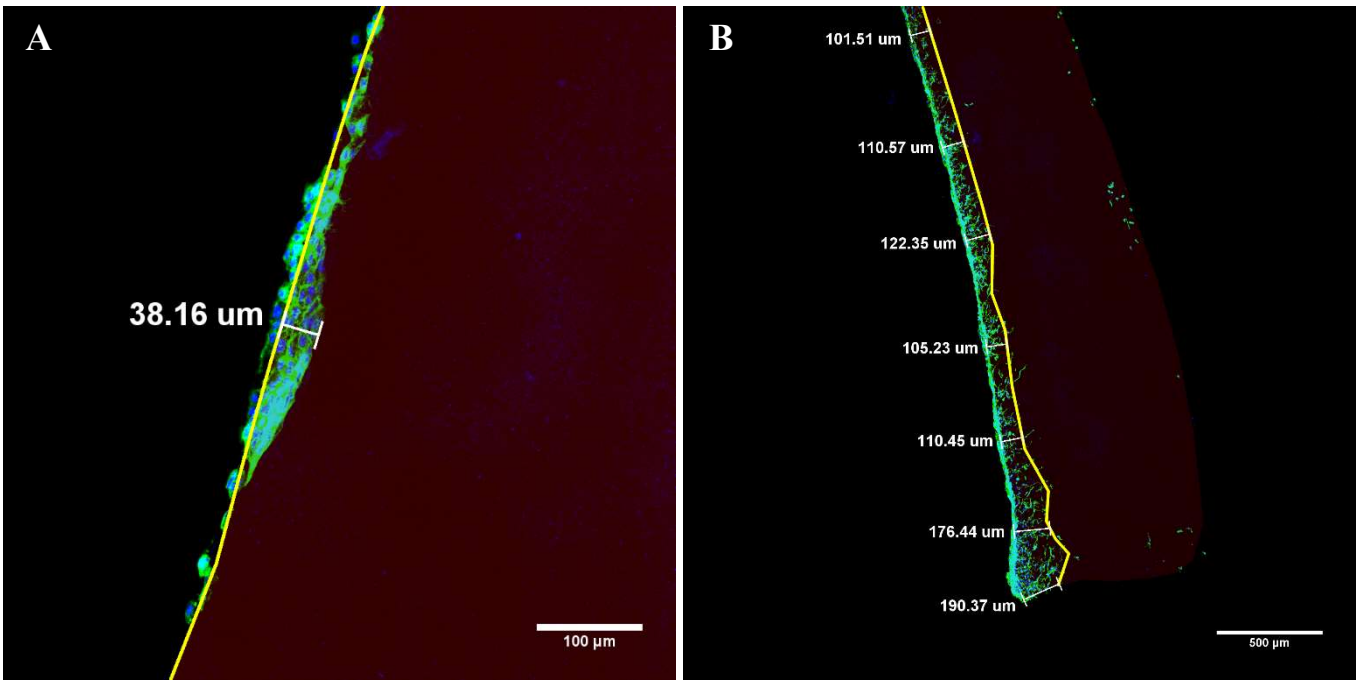

Figure 11: Cell infiltration. Gel outlined with yellow line and filled with red shading, Green is Actin, Blue is DAPI (nuclei) A: Nondegraded, Nonporous gel, 10x B: Partially degraded, Nonporous, 4x

4 Conclusion

One of the main themes of this work is reproducibility and seeking out points of experimental design that may me be improved. From rheological and void fraction results, it is clear that consistency was accomplished for the gel creation process. Furthermore, a high school student in the NCSSM summer program was able to perform the same gel creation process to create gel with similar rheological properties (data is shown in this work). Degradation was also very consistent and predictable leading to precise control of partial degradation experiments.

One aspect of the 3D transfection system that was improved was the cell seeding method. Use of forced fluid flow through the porous network of a gel was immensely more efficient in seeding cells to the innermost regions of the gels. Measuring the transfection of a 3D culture using the new seeding technique will be exciting.

Finally, partial degradation appears to have been effective in its ability to enhance transfection and cell infiltration into the gel. The precise mechanism for enhanced transfection is still to be determined though. As mentioned previously, DNA leeching from the gel to surrounding tissue will still enhance healing nonetheless. If the internal cells are the only transfection target, leeching DNA could become an issue. DNA release was attempted to be measured; however, vastly differing initial results combined with administration complications prevented follow-up experiments, thus concrete conclusions regarding DNA and its interaction with a partially degraded gel could not be made. Cell infiltration, on the other hand, is clearly seen to be improved by partial degradation.

Regarding the degradation halt experiments, perhaps a prudent experiment would be to perform the same halting procedure but include periodic rheological measurements (e.g. collect G' at 12, 24, 36 hours). If all gel degradations are inhibited similarly, their respective storage modulus should remain fairly constant between collection points so even if the higher pH condition is appearing to continue to degrade at 4℃, no actual chains are being cut; rather, some labeled fragments are seeping into the supernatant.

The next step would be to use the more effective seeding techniques to place cells into CnE loaded porous gels and evaluate the transfection rates with and without partial degradation.

The scientific community can often be quite competitive with an enormous emphasis on discovery, potentially leading to what is termed 'bad science.' Overall, this work demonstrates how careful, step-wise approaches to difficult problems can result in robust system capable of being replicated by non-experts to aid in the progression of human society; which, in the end, is the goal of science.

References

1. *National Diabetes Statistics Report, 2017*, D.o.D. Translation, Editor. 2017. p. 20.

2. Dreifke, M.B., A.A. Jayasuriya, and A.C. Jayasuriya, *Current wound healing procedures and potential care.* Mater Sci Eng C Mater Biol Appl, 2015. **48**: p. 651-62.

3. Peppas, N.A., et al., *Hydrogels in Biology and Medicine: From Molecular Principles to Bionanotechnology.* Advanced Materials, 2006. **18**(11): p. 1345-1360.

4. Rice, J.J., et al., *Engineering the regenerative microenvironment with biomaterials.* Adv Healthc Mater, 2013. **2**(1): p. 57-71.

5. Howard M. Kimmel, A.G., James Ditata *The Presence of Oxygen in Wound Healing.* Wounds, 2016. **28**(8): p. 264-270.

6. Howard, M.A., et al., *Oxygen and wound care: a review of current therapeutic modalities and future direction.* Wound Repair Regen, 2013. **21**(4): p. 503-11.

7. Dhaliwal, A., V. Oshita, and T. Segura, *Transfection in the third dimension.* Integr Biol (Camb), 2013. **5**(10): p. 1206-16.

8. Lungwitz, U., et al., *Polyethylenimine-based non-viral gene delivery systems.* Eur J Pharm Biopharm, 2005. **60**(2): p. 247-66.

9. Nayerossadat, N., T. Maedeh, and P.A. Ali, *Viral and nonviral delivery systems for gene delivery.* Adv Biomed Res, 2012. **1**: p. 27.

10. Huang YC, R.K., Rice KG, Mooney DJ, *Long-term in vivo gene expression via delivery of PEI-DNA condensates from porous polymer scaffolds.* Human Genome Therapies, 2005. **16**: p. 609-17.

11. Siegman, S., N.F. Truong, and T. Segura, *Encapsulation of PEGylated low-molecular-weight PEI polyplexes in hyaluronic acid hydrogels reduces aggregation.* Acta Biomater, 2015. **28**: p. 45-54.

12. Tokatlian, T., C. Cam, and T. Segura, *Porous hyaluronic acid hydrogels for localized nonviral DNA delivery in a diabetic wound healing model.* Adv Healthc Mater, 2015. **4**(7): p. 1084-91.

13. Huang, Y.C., et al., *Long-term in vivo gene expression via delivery of PEI-DNA condensates from porous polymer scaffolds.* Hum Gene Ther, 2005. **16**(5): p. 609-17.

14. Meilander-Lin, N.J., et al., *Sustained in vivo gene delivery from agarose hydrogel prolongs nonviral gene expression in skin.* Tissue Eng, 2005. **11**(3-4): p. 546-55.

15. S. Dean Allison, M.d.C.M., Thomas J. Anchordoquy, *Stabilization of lipid/DNA complexes during the freezing step of the lyophilization process: the particle isolation hypothesis.* Biochemica et Biophysica Acta, 2000: p. 127-138.

16. Tokatlian, T., C. Cam, and T. Segura, *Non-viral DNA delivery from porous hyaluronic acid hydrogels in mice.* Biomaterials, 2014. **35**(2): p. 825-35.

17. Peyton, S.R., et al., *Marrow-derived stem cell motility in 3D synthetic scaffold is governed by geometry along with adhesivity and stiffness.* Biotechnol Bioeng, 2011. **108**(5): p. 1181-93.

18. Cam, C. and T. Segura, *Chemical sintering generates uniform porous hyaluronic acid hydrogels.* Acta Biomater, 2014. **10**(1): p. 205-13.

19. Dicker, K.T., et al., *Hyaluronan: a simple polysaccharide with diverse biological functions.* Acta Biomater, 2014. **10**(4): p. 1558-70.

20. Eldridge, L., A. Moldobaeva, and E.M. Wagner, *Increased hyaluronan fragmentation during pulmonary ischemia.* Am J Physiol Lung Cell Mol Physiol, 2011. **301**(5): p. L782-8.

21. Gao, F., et al., *Hyaluronan oligosaccharides promote excisional wound healing through enhanced angiogenesis.* Matrix Biol, 2010. **29**(2): p. 107-16.

22. Siiskonen, H., et al., *Hyaluronan synthase 1: a mysterious enzyme with unexpected functions.* Front Immunol, 2015. **6**: p. 43.

23. Taylor, K.R., et al., *Hyaluronan fragments stimulate endothelial recognition of injury through TLR4.* J Biol Chem, 2004. **279**(17): p. 17079-84.

24. Tokatlian, T., et al., *Design and characterization of microporous hyaluronic acid hydrogels for in vitro gene transfer to mMSCs.* Acta Biomater, 2012. **8**(11): p. 3921-31.

25. Huang, Y.C., et al., *Bone regeneration in a rat cranial defect with delivery of PEI-condensed plasmid DNA encoding for bone morphogenetic protein-4 (BMP-4).* Gene Ther, 2005. **12**(5): p. 418-26.

26. Bellis, S.L., *Advantages of RGD peptides for directing cell association with biomaterials.* Biomaterials, 2011. **32**(18): p. 4205-10.

27. Maheshwari, G., et al., *Cell adhesion and motility depend on nanoscale RGD clustering.* Journal of Cell Science, 2000. **113**(10): p. 1677-1686.

28. Murphy, C.M., M.G. Haugh, and F.J. O'Brien, *The effect of mean pore size on cell attachment, proliferation and migration in collagen-glycosaminoglycan scaffolds for bone tissue engineering.* Biomaterials, 2010. **31**(3): p. 461-6.

29. Collins, M.N. and C. Birkinshaw, *Investigation of the swelling behavior of crosslinked hyaluronic acid films and hydrogels produced using homogeneous reactions.* Journal of Applied Polymer Science, 2008. **109**(2): p. 923-931.

30. Marizza, P., et al., *Synthesis and characterization of UV photocrosslinkable hydrogels with poly(N-vinyl-2-pyrrolidone): Determination of the network mesh size distribution.* International Journal of Polymeric Materials and Polymeric Biomaterials, 2016. **65**(10): p. 516-525.

31. Schurz, J., *Rheology of polymer solutions of the network type.* Progess in Polymer Science, 1991. **16**(1): p. 1-53.

32. Zander, Z.K., et al., *Control of Mesh Size and Modulus by Kinetically Dependent Cross-Linking in Hydrogels.* Adv Mater, 2015. **27**(40): p. 6283-8.

33. Jan Ellenberg, E.D.S., Jorge E. Moreira, Carolyn L. Smith, John F. Presley, Howard J. Worman, and Jennifer Lippincott-Schwartz, *Nuclear Membrane Dynamics and Reassembly in Living Cells: Targeting of an Inner Nuclear Membrane Protein in Interphase and Mitosis.* Journal of Cell Biology, 1997. **138**(6): p. 1193-1206.

34. Kang, M., et al., *Simplified equation to extract diffusion coefficients from confocal FRAP data.* Traffic, 2012. **13**(12): p. 1589-600.

35. Soumpasis, D.M., *Theoretical Analysis of Fluorescence Photobleaching Recovery Experiments.* Biophysics Journal, 1983. **41**: p. 95-97.

36. Yu Cheng, R.K.P.h., *Diffusion of Mesoscopic Probes in Aqueous Polymer Solutions Measured by Fluorescence Recovery after Photobleaching.* Macromolecules, 2002. **35**: p. 8111-8121.

37. Amsden, B., *Solute Diffusion within Hydrogels. Mechanisms and Models.* Macromolecules, 1998. **31**: p. 8382-8395.

38. Holt, B., A. Tripathi, and J. Morgan, *Viscoelastic response of human skin to low magnitude physiologically relevant shear.* J Biomech, 2008. **41**(12): p. 2689-95.

39. Sobral, J.M., et al., *Three-dimensional plotted scaffolds with controlled pore size gradients: Effect of scaffold geometry on mechanical performance and cell seeding efficiency.* Acta Biomater, 2011. **7**(3): p. 1009-18.

40. Teisuke Furuya, S.Y., Yoshishito Shimoyama, Michio Fujihara, Naohiko Morishima, Kenzo Ohtsuki, *Biochemical Characterization of Glycyrrhizin as an Effective Inhibitor for Hyaluronidases from Bovine Testis.* Biol. Pharm. Bull., 1997. **20**: p. 973-977.

41. Tomohara, K., et al., *Interpreting the behavior of concentration-response curves of hyaluronidase inhibitors under DMSO-perturbed assay conditions.* Bioorg Med Chem Lett, 2016. **26**(13): p. 3153-3157.

42. Fu, Y., et al., *Glycyrrhizin inhibits the inflammatory response in mouse mammary epithelial cells and a mouse mastitis model.* FEBS J, 2014. **281**(11): p. 2543-57.

43. Kim, K.J., et al., *The anti-angiogenic activities of glycyrrhizic acid in tumor progression.* Phytother Res, 2013. **27**(6): p. 841-6.

44. Nusgens, B.V., et al., *Topically applied vitamin C enhances the mRNA level of collagens I and III, their processing enzymes and tissue inhibitor of matrix metalloproteinase 1 in the human dermis.* J Invest Dermatol, 2001. **116**(6): p. 853-9.

45. Vadim Ivanov, S.I., Tatiana Kalinovsky, Aleksandra Niedzwiecki, Matthias Rath, *Inhibition of collagen synthesis by select calcium and sodium channel blockers can be mitigated by ascorbic acid and ascorbyl palmitate.* American Journal of Cardiovascular Disease, 2016. **6**: p. 26-35.